Physical mechanisms of conduction-to-keyhole transition in laser welding and additive manufacturing processes

Yaasin A. Mayi, Patrice Peyre, Michel Bellet, Remy Fabbro, Morgan Dal

▶ **To cite this version:**

Yaasin A. Mayi, Patrice Peyre, Michel Bellet, Remy Fabbro, Morgan Dal. Physical mechanisms of conduction-to-keyhole transition in laser welding and additive manufacturing processes. Optics and Laser Technology, 2022, 158 part A, pp.108811. 10.1016/j.optlastec.2022.108811 . hal-03898086

HAL Id: hal-03898086
https://hal.science/hal-03898086v1

Submitted on 14 Dec 2022

HAL is a multi-disciplinary open access archive for the deposit and dissemination of scientific research documents, whether they are published or not. The documents may come from teaching and research institutions in France or abroad, or from public or private research centers.

L'archive ouverte pluridisciplinaire **HAL**, est destinée au dépôt et à la diffusion de documents scientifiques de niveau recherche, publiés ou non, émanant des établissements d'enseignement et de recherche français ou étrangers, des laboratoires publics ou privés.

Physical mechanisms of conduction-to-keyhole transition in laser welding and additive manufacturing processes

Yaasin A. Mayi [a,*], Morgan Dal [b], Patrice Peyre [b], Michel Bellet [c], Remy Fabbro [b]

[a] Safran Additive Manufacturing Campus, rue de Touban – BP 90053, 33185 Le Haillan, France
[b] Laboratoire PIMM, Arts et Metiers Institute of Technology, CNRS, Cnam, HESAM University, 151 boulevard de l'Hopital, 75013 Paris, France
[c] Mines Paris – PSL, CEMEF – Centre de Mise en Forme des Matériaux, CNRS UMR 7635, CS10207 rue Claude Daunesse, 06904 Sophia Antipolis Cedex, France

A B S T R A C T

Thermo-hydrodynamic phenomena which take place during laser welding or additive manufacturing processes as laser powder bed fusion, have been investigated for years, but recent advances in X-ray images and *in situ* analysis have highlighted new findings that are still under debate. Conduction-to-keyhole transition, and more broadly, keyhole dynamics, are typical cases, where complex coupling between hydrodynamic and optical problems are involved. In this paper, a keyhole and melt pool model is developed with the software COMSOL Multiphysics®, where laser energy deposition is computed self-consistently thanks to a ray tracing algorithm. The model successfully reproduces experimental findings published in the literature and helps to analyze accurately the role played by the beam trapping phenomenon during the conduction-to-keyhole transition, in both spot welding (*i.e.*, stationary laser illumination) and welding configurations (*i.e.,* with scanning speed). In particular, it is shown that depending on the welding speed, multiple reflections might be either a stabilizing or a destabilizing factor. Understanding these mechanisms is thus a prerequisite for controlling the stability of the melt pools during the joining or the additive manufacturing processes.

1. Introduction

The keyhole (KH) mode refers to a laser-material interaction regime, where the incident laser irradiation is "trapped" by the melt pool, by multiple reflections effect. The incident irradiances involved in joining processes such as welding, or in additive manufacturing technologies such as Laser Powder Bed Fusion (LPBF), are high enough ($\gtrapprox$ 1 MW/cm^2) to vaporize the irradiated metal alloy. A recoil pressure is thus exerted onto the melt pool, which creates a cavity (the KH) at the center of the interaction zone, in which the incident beam gets trapped. The energy coupling of the process is thus "cavity-enhanced" [1], which makes possible to weld sheets of several millimeter thick, or to ensure material continuity between subsequent layers in LPBF.

Whilst the KH increases the process energy efficiency, it also affects the melt flow that takes place in the melt pool. The solid metal fuses and feeds the melt pool at welding speed, through the bead cross section (Fig. 1). The melt is then ejected rearward from the interaction zone, through a liquid thickness that is narrowed by the KH – a fraction of the melt is also lost by evaporation. At steady state, by mass conservation principle, one deduces that the ejection velocity is much higher than the welding speed, depending on the ratio between the seam cross section and the melt section. On this basis, among others, Fabbro [2] extended the so-called "piston model" [3] to calculate self-consistently the KH depth, temperature, melt thickness and ejection velocity, as a function of the process parameters and the material properties.

The above description of the melt flow is rather simple, but it highlights a competition between two antagonistic phenomena that may take place in the melt pool (independently of any other driving forces such as thermocapillary shear stress or friction of vapor plume): (1) KH penetration and (2) KH opening. The recoil pressure promotes KH penetration, and the beam trapping effect enhances it. Simultaneously, the KH opens as a result of the above-described melt flow, and different driving forces may promote its opening, to the expense of energy coupling (there are less multi-reflections as the cavity gets larger) and potentially, at the expense of KH penetration. During the conduction-to-keyhole transition, this competition occurs, until an equilibrium is eventually found.

Despite the impressive development of numerical simulations dedicated to melt pool and KH dynamics in welding and AM (see Fig. 1 in ref. [4]), this issue has, paradoxically, quite rarely been analyzed from this perspective.

KH penetration mechanisms have been investigated quite early. For

Nomenclature

A_0	Normal absorptance [-]
c_p	Specific heat [J·kg^{-1}·K^{-1}]
C_1	Darcy's penalization constant [kg·m^{-3}·s^{-1}]
C_2	Darcy's penalization constant [-]
f_{liq}	Liquid fraction [-]
I_{abs}	Absorbed irradiance [W·m^{-2}]
k	Thermal conductivity [W·m^{-1}·K^{-1}]
K	Number of reflections per ray [-]
L_m	Latent heat of fusion [J·kg^{-1}]
$\dot{m}$	Ablation flux [kg·m^{-2}·s^{-1}]
Ma_{Kn}	Mach number out of the Knudsen layer [-]
N	Number of rays [-]
p	Pressure [Pa]
p_{atm}	Atmospheric pressure [Pa]
p_{sat}	Saturated vapor pressure [Pa]
P_L	Laser power [W]
r	Radial distance from laser optical axis [m]
R	Universal gas constant [J·mol^{-1}·K^{-1}]
R_L	Laser radius (1/e^2) [m]
t	Time [s]
T	Temperature [K]
T_{sol}	Solidus temperature [K]
T_{liq}	Liquidus temperature [K]
T_m	Mean fusion temperature [K], $T_m = (T_{liq} + T_{sol})/2$
T_v	Vaporization temperature at P_{atm} [K]
T_{Kn}	Temperature out of Knudsen layer [K]
V_I	Interface normal velocity [m·s^{-1}]

Greek letter

α_1	Angular threshold to first multiple reflexions
α_2	Angluar step for the update of the absorbed heat flux
β_R	Retro-diffusion coefficient [-]
γ	Specific heat ratio [-]
ΔT	Fusion / solidification interval [K], $\Delta T = (T_{liq} - T_{sol})/2$
κ	Interface curvature [m^{-1}]
μ	Dynamic viscosity [Pa·s]
ρ	Density [kg·m^{-3}]
σ	Surface tension [N·m^{-1}]
$\partial\sigma/\partial T$	Thermocapillary coefficient [N·m^{-1}·K^{-1}]
$\varnothing_{Kn}$	Help function

Vectors

$\vec{n}$	Normal to metal interface [-]
$\vec{u}$	Velocity field [m·s^{-1}]

Superscripts

eq	Equivalent
l	Liquid
s	Solid

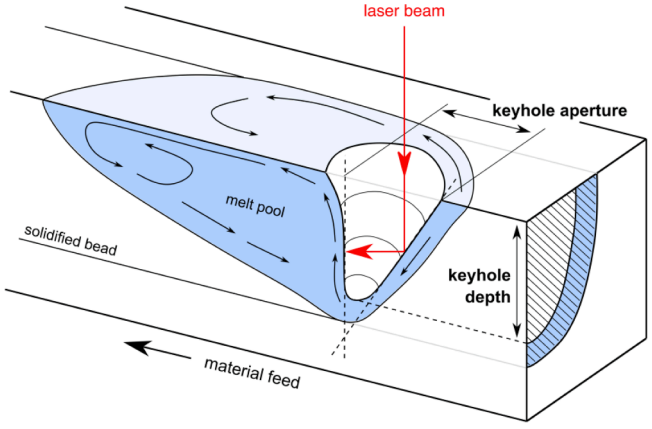

Fig. 1. Schematics of keyhole.

instance, Ki et *al.* [5], Lee et *al.* [6] or even Medale et *al.* [7] simulated the influence of multiple reflections on stability and coupling efficiency of spot welding (*i.e.*, stationary laser irradiation). These works were not or hardly experimentally validated. But recent advances in melt pool *in situ* visualization by X-ray radiography [8] and online absorptance measurement [1,9,10], demonstrated the causal relationship between the KH shape and the coupling mechanisms that were then suggested. These experimental works, in turn, constituted a valuable database for more recent modelers, to validate their numerical simulations and to further analyze and quantify the mechanisms that lead to conduction-to-keyhole transition in stationary laser configuration [11–13].

KH stability and induced melt flow have also been widely investigated in the context of welding, and more recently, in the field of LPBF. For instance, Courtois et *al.* [14] simulated destabilization of KH rear wall by the vapor plume. Pang et *al.* [15] investigated the link between KH oscillations and vapor plume fluctuations. Tang et *al.* [16], Bayat et *al.* [17] or Yuan et *al.* [18] studied pore formation as a result of KH collapse. Tang et *al.* [19] also produced one of the few simulations where the humping phenomenon is well reproduced. Wang and Zou [20] compared conduction and KH modes in LPBF by means of simplified thermal model. Liu et *al.* [21] investigated the effect of laser defocusing on melt pool fusion modes. Other works have also relied on X-ray imaging to validate the simulated KH morphology accurately [22,23] or to illustrate how the reflected irradiation might destabilize the KH rear front at steady state [24].

In reviewing the literature on KH simulation, it is clear that some authors have investigated the dynamic of KH formation in static configuration (which is logical, since laser spot welding is a transient process by nature). However, to the best of our knowledge, very few looked at conduction-to-keyhole transition in scanning mode: most authors investigated the KH shape and stability at steady state. Nevertheless, examination of conduction-to-keyhole mechanisms allows understanding why some process conditions are more unstable than others. For instance, Fabbro [2] recently demonstrated that the unstable conduction-to-keyhole window necessarily enlarges when decreasing the material absorptance. Also, the conduction-to-keyhole mechanisms are particularly relevant to LPBF process, which is often carried out in intermediate melting mode. Therefore, the goal of the present paper is to put a special emphasis on the role played by multiple reflections at the onset of KH formation.

First, a numerical model developed with COMSOL Multiphysics® is introduced. It is then experimentally validated in spot welding configuration thanks to data extracted from the literature, and KH formation mechanisms are introduced. Finally, conduction-to-keyhole transition is analyzed in welding configuration (*i.e.,* with scanning speed). The simulated KH depth and absorptance are validated, and the results obtained in three welding process settings are discussed, in the light of the competing mechanisms described above.

2. Computational model

2.1. Governing equations

2.1.1. Laser beam energy deposition

Laser irradiance is computed with the ray tracing method. N rays are initialized in the computational domain, with a normal probabilistic distribution $\mathscr{P}(r)$:

$$\mathscr{P}(r) = \exp\left(-2\frac{r^2}{R_L^2}\right) \tag{1}$$

where $r = \sqrt{x^2 + y^2}$ is the radial distance to the laser optical axis and R_L is the $1/e^2$ laser spot radius. Each ray carries equal fraction $(1/N)$ of the laser incident power P_L, and interacts with the material surface according to Snell-Descartes law. At first interaction, the irradiated material is flat; thus, multiple reflections do not occur. Therefore, the absorbed heat flux I_{abs} is:

$$I_{abs}(t=0) = A_0\frac{2P_L}{\pi R_L}\exp\left(-2\frac{r^2}{R_L^2}\right)cos(\theta) \tag{2}$$

where A_0 is the material absorptance (supposed constant) and θ is the laser incident angle (relative to the surface normal). Then, when multiple reflections occur, the resulting absorbed flux accounts for the contribution of each reflected ray [7]:

$$I_{abs} = \sum_i^N \sum_j^K A_0 I_{ij}(r, z, \theta) \tag{3}$$

where K is the number of reflections per ray and I_{ij} is the irradiance of the i^{th} ray at the j^{th} interaction.

2.1.2. Heat transfer

The governing equation for energy conservation is computed as:

$$\rho c_p^{eq}\frac{\partial T}{\partial t} + \rho c_p^{eq}(\vec{u}\cdot\vec{\nabla}T) = \vec{\nabla}\cdot(k\vec{\nabla}T) \tag{4}$$

where c_p, k and ρ are respectively the specific heat, the thermal conductivity, and the density. Enthalpy of fusion L_m of the metal alloy (Ti-6Al-4V) is accounted for through an equivalent specific heat c_p^{eq}:

$$c_p^{eq} = (1 - f_{liq})c_p^s + f_{liq}c_p^l + \frac{L_m}{\sqrt{\pi\Delta T^2}}exp\left[-\frac{(T - T_m)^2}{\Delta T^2}\right] \tag{5}$$

where c_p^s and c_p^l are the specific heats of the solid and liquid phases respectively, $\Delta T = (T_{liq} - T_{sol})/2$ and $T_m = (T_{liq} + T_{sol})/2$. Then, laser heat flux is counterbalanced by vaporization losses at liquid/vapor interface:

$$k\vec{\nabla}T\cdot(-\vec{n}) = I_{abs} - \dot{m}L_v \tag{6}$$

where L_v is the latent heat of vaporization. During the fusion, heat lost by natural convection and by radiation are negligible compared to vaporization losses. Also, the ablation flux $\dot{m}$ is computed as [25]:

$$\dot{m} = \sqrt{\frac{M}{2\pi RT_s}}p_{sat}(T_s) + \beta_R\sqrt{\frac{M}{2\pi RT_{Kn}}}p_{sat}(T_{Kn})f(\varnothing_{Kn}) \tag{7}$$

$$f(\varnothing_{Kn}) = \sqrt{\pi}\varnothing_{Kn}erfc(\varnothing_{Kn}) - exp(-\varnothing_{Kn}^2) \tag{8}$$

$$\varnothing_{Kn} = \frac{\gamma}{2}Ma_{Kn}^2 \tag{9}$$

where M is the molar mass, Ma_{Kn} and T_{Kn} are the Mach number and the temperature out of the Knudsen layer, T_s is the temperature at the melt surface, β_R is the *retro*-diffusion coefficient and γ is the specific heat ratio. In addition, the saturated vapor pressure p_{sat} is computed thanks to the Clausius-Clapeyron law:

$$p_{sat}(T) = p_{atm}exp\left[\frac{ML_v}{RT_v}\left(1 - \frac{T_v}{T}\right)\right] \tag{10}$$

where p_{atm} is the atmospheric pressure, and T_v is the boiling temperature at atmospheric pressure.

2.1.3. Fluid flow

Navier-Stokes equations are solved in the metal phase, which behaves as a Newtonian incompressible fluid:

$$\vec{\nabla}\cdot\vec{u} = 0 \tag{11}$$

$$\rho_l\frac{\partial\vec{u}}{\partial t} + \rho_l(\vec{u}\cdot\vec{\nabla})\vec{u} = \vec{\nabla}\cdot\{-pI + \mu[\vec{\nabla}\vec{u} + (\vec{\nabla}\vec{u})^T]\} - C_1\frac{(1 - f_{liq})^2}{f_{liq}^3 + C_2}\vec{u} \tag{12}$$

where ρ_l is the density of the melt, and μ is the dynamic viscosity. The last term on the right-hand side of Eq. (12) corresponds to a Darcy's term used to penalize the velocity field in the solid phase [26] (f_{liq} is the liquid fraction, and C_1 and C_2 are two calibrated numerical constants). Then, at liquid/gas interface, stress balance gives:

$$(-pI + \mu[\vec{\nabla}\vec{u} + (\vec{\nabla}\vec{u})^T])\cdot\vec{n} = -(p_s - p_{atm})\vec{n} + \sigma\kappa\vec{n} + \frac{\partial\sigma}{\partial T}\vec{\nabla}_s T \tag{13}$$

where σ is the surface tension, κ is the liquid/gas interface curvature, $\vec{n}$ is the normal to the interface and $\partial\sigma/\partial T$ is the thermocapillary coefficient. The total pressure p_s exerted onto the melt pool surface due to vaporization is derived from Eq. (14)-(15).

$$p_s = \frac{1}{2}P_{sat}(T_s) + \beta_R P_{sat}(T_{Kn})g(\varnothing_{Kn}) \tag{14}$$

$$g(\varnothing_{Kn}) = \left(\frac{1}{2} + \varnothing_{Kn}^2\right)erfc(\varnothing_{Kn}) - \frac{\varnothing_{Kn}}{\sqrt{\pi}}exp(-\varnothing_{Kn}^2) \tag{15}$$

2.1.4. Interface tracking

Liquid/gas interface is tracked with the Arbitrary Lagrangian Eulerian (ALE) method. The boundary is discretized with a conformed mesh, and its normal velocity is computed as a function of that of the melt:

$$V_I = \vec{u}\cdot\vec{n} \tag{16}$$

Then, mesh displacement is propagated throughout the domain, following the Yeoh smoothing method [27], to minimize elements distortion.

The ALE method guarantees a more accurate treatment of the boundary conditions than Eulerian methods, such as Level-Set [4]. However, topological changes such as pore formation are not managed, except at the cost of interface reconstruction, which is not natively supported in COMSOL Multiphysics®. This limitation is not a problem here because the work is focused on the conduction-to-keyhole transition, where the risk of pore formation is low.

2.2. Ray tracing algorithm

No method was available in COMSOL Multiphysics® to compute self-consistently the laser-material interaction with the ray tracing method. Therefore, a dedicated JAVA® algorithm was developed with the help of the COMSOL® Application Builder. Detailed description and verification of the algorithm were presented in previous works [28,29]. Here, the method is summarized as follows:

- **Step 1:** The multiphysical problem is initialized. The thermo-hydrodynamic problem is computed without ray tracing, until the maximum variation of the interface angle (driven by the recoil pressure) reaches locally a first threshold α_1. α_1 corresponds to the

Table 1
Thermophysical properties of Ti-6Al-4V (temperature ranges in kelvin). Properties marked with an asterisk are those of pure titanium.

Properties (units)	Consolidated	Extrapolated
A_0 (-)	0.33 (calibrated)	–
c_p ($J{\cdot}kg^{-1}{\cdot}K^{-1}$)	$298 \leq T \leq 2173$[33]	$2173 \leq T \leq 4000$
k ($W{\cdot}m^{-1}{\cdot}K^{-1}$)	$298 \leq T \leq 2173$[33]	$2173 \leq T \leq 4000$
L_m ($J{\cdot}kg^{-1}$)	$2.86{\cdot}10^5$ [33]	–
L_v ($J{\cdot}kg^{-1}$)	$8.90{\cdot}10^{6*}$ [34]	–
M ($kg{\cdot}mol^{-1}$)	0.0479 (calculated)	–
T_{sol} (K)	1878 [35]	–
T_{liq} (K)	1923 [35]	–
T_v (K)	3558* [34]	–
γ (-)	1.67 (assumed)	–
ρ ($kg{\cdot}m^{-3}$)	$298 \leq T \leq 2173$[33]	$2173 \leq T \leq 4000$
σ ($N{\cdot}m^{-1}$)	1.38 [36]	–
$\partial\sigma/\partial T$ ($N{\cdot}m^{-1}{\cdot}K^{-1}$)	$-0.31{\cdot}10^{-3}$ [36]	–

angle at which the incident rays would be reflected toward the melt pool for the first time. Therefore, the absorbed heat flux is no longer described correctly by the Eq. (2) and must be updated.

- **Step 2:** The optical problem is computed in the latest geometrical configuration (end of step 1), in order to account for the contribution of the multi-reflected rays in the absorbed heat flux (Eq. (3)). Calculation stops when all rays carry a residual power lower than one thousandth of their initial power (like in Touvrey-Xhaard's work [30]). Note that the total number of rays (here $N = 50\,000$) is chosen to make a trade-off between the spatial resolution of the absorbed irradiance (that should be maximized) and the computational time of a single ray tracing calculation (that should be minimized). Detailed study is available in ref. [29].
- **Step 3:** The thermo-hydrodynamic problem is restarted from the latest configuration (end of step 1) with the absorbed heat flux updated at step 2, until the maximum angle variation reaches locally a second threshold α_2. α_2 is the angular step, which controls the update frequency. Calculation then stops. The numerical solutions obtained at the first and third steps are concatenated and the second and third steps are reiterated until the final time step is reached.

The advantage of this method (based on an angular step) compared to algorithms based on regular updates, is that the update frequency adapts to the fluctuation of the KH. This saves computational time, especially by limiting the number of updates when the melt pool is very stable. However, the main limitation is that fluctuations below the threshold α_2 are somehow filtered by the algorithm. This prevents, for instance, a rigorous quantitative study of the KH frequency signature, as carried out numerically by Geiger et *al.* [31] or experimentally by Allen et *al.* [10].

Finally, note that when α_2 tends toward 0° (all other things being equal), the simulated time-to-keyhole converges toward as single value [28]. Furthermore, α_2 must be chosen to make a trade-off between the temporal resolution of the algorithm (that should be maximized, to track the time-to-keyhole accurately) and the computational time (which increases with the number of updates).

Table 2
Numerical constants.

Numerical constants (unit)	Values	References
C_1 ($kg{\cdot}m^{-3}{\cdot}s^{-1}$)	10^6	[4]
C_2 (-)	10^{-6}	[4]
N (-)	50,000	[28]
α_1 (°)	35	[28]
α_2 (°)	10 (static), 20 (scanning)	[28]

2.3. Thermophysical properties and numerical constants

The simulations are performed with the thermal properties of titanium alloy Ti-6Al-4V (Ti64). Temperature-dependent properties are implemented in the thermal model. The references used for the consolidated values are reported in the Table 1. The numerical constants are also reported in the Table 2.

Importantly, the local absorptance A_0 of Ti64 is assumed constant. It has been calibrated to 0.33 in a preliminary work [28], to get time-to-keyhole values in agreement with experimental data published by Cunningham et *al.* [8].

2.4. Numerical considerations

Detailed numerical configuration (computational domain, mesh, solver setup) was described in a dedicated paper [28]. Here, the main numerical considerations are summarized in Table 3.

First, the static problem is computed assuming a cylindrical symmetry, with adiabatic lateral boundaries. The mesh is composed of triangular elements, refined at the liquid/gas interface (at laser spot position) down to 1 μm. The total number of Degrees of Freedom (DOF) is 50 000.

Secondly, in scanning configuration, a symmetry plan is considered at the intersection of the scan path and the laser optical axis. Also, note that the simulations are run in quasi-steady state configuration (*i.e.,* the material is translating in the fixed laser beam frame). The material enters the computational domain at fixed temperature of 293 K (the other boundaries are adiabatic). The parallelepipedal domain is composed of tetrahedral elements, refined at the liquid/gas interface, down to 3 μm. There is a total of 600 000 DOF.

Finally, in both static and scanning configurations, time step is set at 1 μs. However, it is lowered if needed, by the automatic time stepping algorithm pre-implemented in COMSOL®, to ensure a better numerical convergence.

3. Experimental data

Reference experimental data, extracted from literature, are exploited to validate the presented thermo-hydrodynamic model. These are: (1) transient KH depths measured by Cunningham et *al.* [8], during spot weld experiments, carried out on Ti64 bare plates, (2) steady KH depths measured by the same authors during laser micro-welding experiments performed on the same alloy, and (3) steady KH absorptances, measured by Ye et *al.* [32] during laser micro-welding experiments, carried out on various metal plates (Ti64, Inconel® 625 and 316L stainless steel).

Table 3
Summary of numerical configurations.

Configuration	Hypotheses	Domain size (μm)	Mesh size (μm)	Time step (μs)
Static	Axisymmetric	600 (radius), 300 (depth)	1	1
Scanning	Symmetry, quasi-steady stae	2000 × 500 × 1000	3	1

4. Conduction-to-keyhole transition in spot welding configuration

As mentioned above, KH formation during spot welding has been extensively studied [11–13]. However, there are strong analogies between the static and the dynamic configurations. Therefore, a short recall of these mechanisms is necessary to introduce key notions that will be transposed to welding configuration. This is also an opportunity to validate quantitatively the numerical model in transient regime.

4.1. Qualitative study of conduction-to-keyhole transition mechanisms

Melt pool hydrodynamics during spot welding is simulated in three process configurations (Table 4). The sequence simulated for $P_L = 156$ W is compared to its experimental counterpart in Fig. 2 (the animation is available in the supplementary materials: supplementary video 1).

Four characteristic steps are identified here:

a. "Conduction" mode. The melt pool forms a few dozens of microseconds after the laser is turned on. The maximum temperature at the liquid/gas interface is below the boiling point of the alloy ($T_v = 3558$ K). Therefore, the interaction zone is globally flat (only slightly deflected by the thermocapillary shear stress), and the incident beam is absorbed only once.
b. "Forced conduction" mode [2]. The maximum temperature at the liquid/gas interface exceeds the boiling point. The recoil pressure is exerted downwards, onto the melt pool, and a shallow melt pool deflection forms. However, this deflection is not deep enough to trap the incidents rays. Hence, the incident beam is still absorbed once.
c. Melt pool destabilization. The deflection continues to deepen in a very stable manner, until a portion of the liquid/gas interface reaches an inclination of 45° (relative to the laser axis). A fraction of the incident beam is then reflected horizontally. The lateral parts of the melt are thus irradiated twice: the local temperature exceeds the boiling point, and the recoil pressure, which is then exerted radially, makes the melt pool oscillate. The latter continues to deepen, until a fraction of the incident beam is deflected bottomward by the wavy melt pool. The absorbed irradiance increases locally by an order of magnitude (as shown in ref. [12]), which initiates the KH mode.
d. Initiation of KH mode. The deflection takes its characteristic "V-shape" quasi-instantaneously (in ten microseconds in the present case). Consequently, the incident beam is trapped, which increases the coupling efficiency of the process: the KH apparent absorptance rises from 0,33 (*i.e.*, the material absorptance) to 0,55. Note that the simulated "tip effect" at the KH bottom is exaggerated compared to the experimental observations. This is probably due to the fact that vapor plume expansion – which would mitigate this effect by exerting a pressure on the KH wall – is not simulated here.

After the KH is initiated, there is a fifth regime (not simulated here due to the limits of the ALE method) where the KH is very unstable, and collapses periodically even though the laser is still irradiating the metal [8,13].

4.2. Quantitative validation of the model

The previous qualitative analysis demonstrates that the developed model is able to simulate four melt pool stages relevant to KH formation, at characteristic times close to the experimental data. The numerical and experimental KH depths vs time curves are then compared in Fig. 3a.

Table 4
Spot welding parameters.

Process parameter	Value(s)
Laser beam diameter (μm)	140
Laser power (W)	156, 182, 234

First, considering the red curve for $P_L = 156$ W, the four stages described above are noticeable: the liquid/gas interface is flat during the first 100 μs (*i.e.*, "conduction" mode), then the deflection deepens smoothly during the next 600 μs (*i.e.*, "forced conduction" mode), afterward, the position of the deflection oscillates, but continues to deepen at the same mean rate (*i.e.*, destabilization of the melt pool), until the KH mode is sharply initialized, between $t = 1034$ μs and $t = 1044$ μs (Fig. 2c-d). Then the experimental curve shows high amplitude oscillations, revealing a strong KH instability.

However, the simulated "conduction" regime is shorter than the experimental one. Provided the numerical and experimental spot sizes and laser powers are identical (*i.e.*, if in ref. [8] these input parameters have been characterized in the actual experimental conditions), this difference might be the direct consequence of the assumption made on A_0. The simulated "forced conduction" regime starts about 100 μs too early, which means that the value of $A_0 = 0.33$ is too high to be representative of the fusion at lower temperatures – this is the case, indeed, because Ye et *al.* [32] measured a minimum absorptance of 0.26 for liquid Ti64, which is 21 % lower than our calibrated value. However, during the "forced conduction" phase, both numerical and experimental curves are parallel, which indicates that $A_0 = 0.33$ is a fairly good estimation of the absorptance in this regime – since the drilling velocity is determined by the absorbed irradiance [3]. This is also interesting to note that the shift described above reduces as the incident laser power increases, even though calibration of absorptance has been performed once. This is logical: the error is more important as the melt pool stays in "conduction" regime longer; thus, at lower absorbed irradiances.

Also, some authors use the Fresnel law to estimate the material absorptance, rather than a calibrated one. This is, for instance, the case of Wang et *al.* [11], who reproduced the same experimental dataset, using the refractive indexes of pure titanium. However, at normal incidence, this yields to an absorptance value of 0.39, which reinforces the gap between the numerical and experimental results. Actually, in our case, the gap is reasonable, considering the fact that the material absorptance has been calibrated to fit the experimental time-to-keyhole value only: calibration did work with, in all three cases, an error of less than 50 μs in the time-to-keyhole estimate.

Also, note that the hypothesis made on the boiling temperature (assumed equal to that of pure titanium) has an impact on the predicted time-to-keyhole value. In the literature, different values of T_v are taken for Ti64 alloy (for instance, 3591 K in Medale et *al.* [7], or 3315 K in Wang et *al.* [11]). T_v is the vaporization threshold: if its actual value is lower than that of pure titanium, then in the simulation, vaporization occurs later than expected. Nevertheless, in our results, this bias is compensated by the calibration made on the material absorptance, fixed to match the experimental time-to-keyhole values.

Finally, the contours of the liquid/gas interface at each of the four stages, are superimposed on a single map, in Fig. 3b. This view is instructive, because it shows that during stationary irradiation, conduction-to-keyhole transition occurs at constant cavity aperture. In spot welding, the aperture is imposed by the laser spot diameter, as it fixes the area of the evaporating zone. With a top-hat laser beam (*i.e.*, homogeneous irradiance distribution), the KH aperture is roughly equal to the beam diameter [2]; whereas with a Gaussian beam, the KH aperture is smaller than the $1/e^2$ diameter usually considered, here about 100 μm (for a beam diameter of 140 μm).

Therefore, conduction-to-keyhole transition logically occurs at constant deflection depth (here ~ 25 μm), independently to the laser power, as shown in Fig. 3a. Actually, this phenomenon reduces to a geometrical problem, where, for a given KH aperture, the transition occurs when the depth-to-aperture ratio reaches a critical value, here ~ 0.25.

In scanning configuration, the same physical mechanisms and the same formation steps are found. However, competition between KH penetration and KH opening must be accounted for, to understand the conduction-to-keyhole transition.

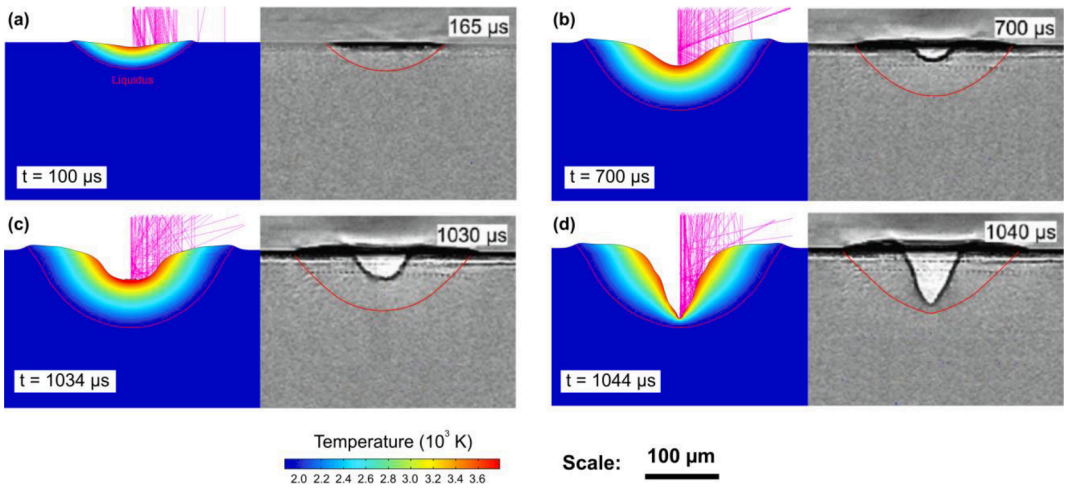

Fig. 2. Comparison of simulated and observed keyhole formation sequences. **a.** "Conduction" mode. **b.** "Forced conduction" mode. **c.** Destabilization of the melt pool at beginning of laser multiple reflections. **d.** Initiation of the KH mode. X-ray images extracted from Cunningham et *al.* [8]. Reprinted with permission from AAAS.

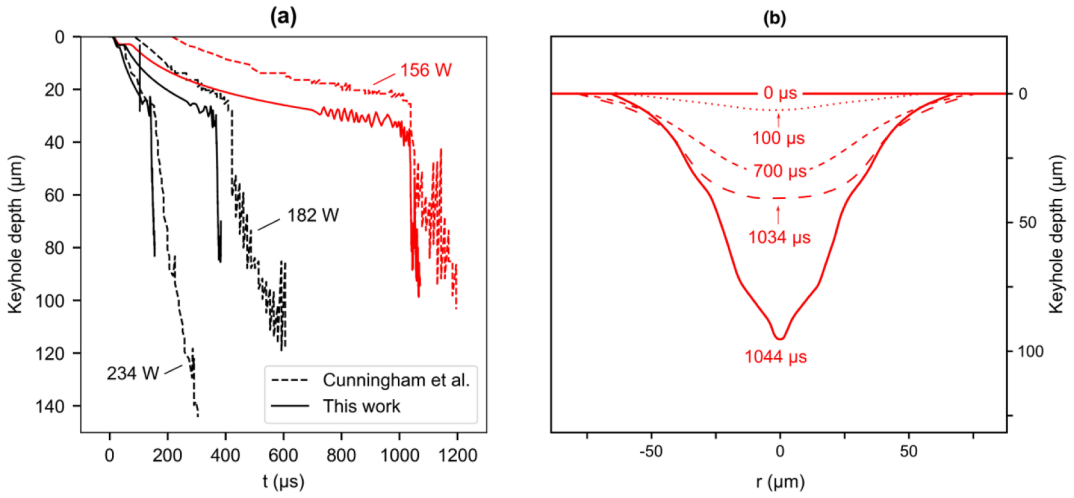

Fig. 3. a. Comparison of numerical (dotted lines) and experimental (solid lines) KH depth vs time cures. **b.** Contours of the liquid/gas interface during the KH formation steps for $P_L = 156$ W.

Table 5
Welding parameters.

Process parameter	Value(s)
Laser beam diameter (µm)	140
Scanning speeds (mm/s)	400, 700, 1000
Laser powers (W)	125 → 400

5. Conduction-to-keyhole transition in scanning configuration

5.1. Quantitative validation of the model

5.1.1. KH depths at steady state

Laser welding experiments are now simulated in sixteen process configurations (Table 5). To improve the numerical stability, note that the power supply has been ramped up with the term $[1 - exp(t/\tau)]$, where $\tau = 70$ µs. This has no consequence on the predicted KH depth at steady state, but this will be taken into consideration during the analysis of the conduction-to-keyhole process.

First, the predicted KH depth at steady state for three welding speed and various incident powers are compared in Fig. 4a, to the experimental results published by Cunningham et *al.* [8] obtained with comparable process parameters. Globally, the model finds right trends and values: most simulated KH depths at steady state are estimated within a ± 10 % margin around the experimental data, especially at higher powers. However, at higher scanning speeds (700 mm/s and 1000 m/s) and lower incident powers, the model overestimates the deflection depths by 15–20 %. This is consistent with the observations made for the spot welding cases, where the deflection depths were also overestimated in "forced conduction" mode. Therefore, the same explanation holds.

Then, at first order, the deflection depth follows a linear trend with the laser power, as highlighted by Cunningham et *al.* [8]. The linear relationship between the KH depth and the laser power is quite classical in laser welding [37]. However, the numerical results do show a slight slope change at a constant depth of ~ 50 µm, independently of the welding speed. This transition is less significant as the welding speed increases. Of course, at higher welding speeds (700 mm/s and 1000 mm/s), this transition is exaggerated by the model since the deflection depths are overestimated. But at 400 mm/s, this transition is clearly visible in both experimental and numerical results. The experimental results found in this configuration are therefore plotted separately in Fig. 4b, and compared to the simulations results obtained with and without the ray tracing algorithm (*i.e.*, with and without accounting for

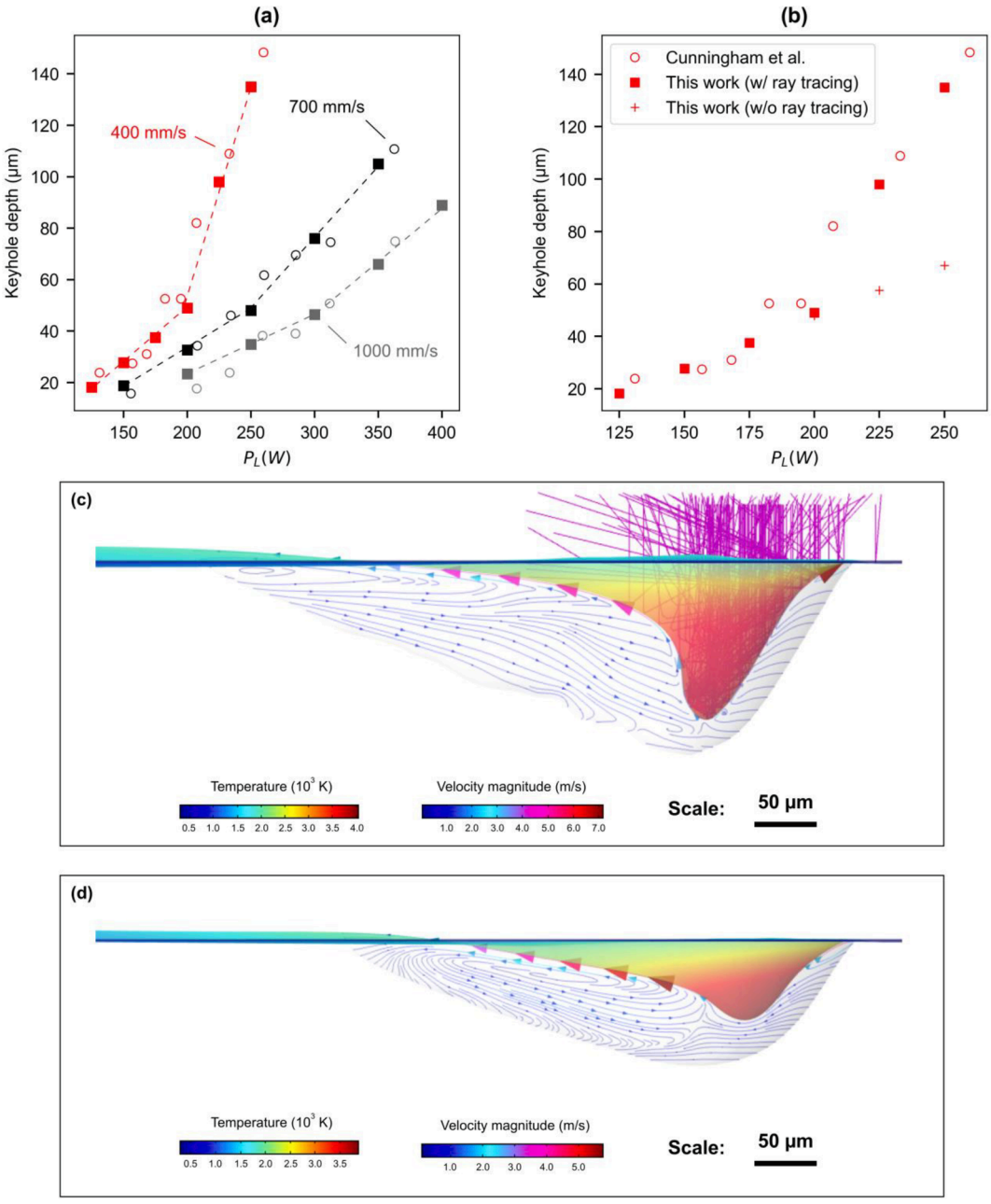

Fig. 4. **a.** Comparison of simulated (solid boxes) and experimental (empty circles) KH depth at steady state vs laser power. **b.** Focus on $V_L = 400$ mm/s: comparison of KH depth versus power, simulated with (solid boxes) and without (crosses) ray tracing, to experimental data (empty circles). The experimental data are extracted form Cunningham et *al.* [8]. **c.** KH and melt pool shape simulated with ray tracing for $V_L = 400$ mm/s and $P_L = 250$ W. **d.** KH and melt pool shape simulated without ray tracing for $V_L = 400$ mm/s and $P_L = 250$ W.

the beam trapping effect, respectively).

Both numerical results match quite well the experimental ones, between 125 W and 200 W. This means that no beam trapping occurs. Hence, the melt pool is still in "forced conduction" mode. However, beyond 200 W, the two sets of numerical results diverge as the incident power increases. The KH depths predicted with ray tracing follow the experimental findings accurately, whereas the ones simulated without ray tracing follow the initial linear trend. In short, this means that the KH threshold is reached at this point, with a threshold depth of ~ 50 μm, that is twice that of the static configuration.

In laser welding, with a top-hat beam, it is generally accepted that the KH threshold is reached when the KH-depth-to-focal-spot-ratio (also called aspect ratio) exceeds the value of one. Accepting this definition, we then demonstrate here that for a Gaussian beam, the $1/e^2$ diameter – which is often taken arbitrarily as characteristic diameter – is not relevant, and even incorrect. A more relevant diameter would be the characteristic width which contains 50 % of the incident energy: $D_{1.35\sigma} = 2{\cdot}0.67\sigma = 47\mu m$ (σ being here the standard deviation of the normal distribution). In other terms, $D_{1.35\sigma}$ contains the "effective" fraction of the incident energy.

Finally, to emphasize the importance of beam trapping in laser welding, the melt pool and KH shapes predicted with and without ray tracing are compared in Fig. 4c-d, when $V_L = 400$ mm/s and $P_L = 250$ W. The difference is clear: there is a factor two between the depth estimates. In the first case (with ray tracing), a KH is formed, the incident rays irradiate mainly the front KH and are reflected bottomward. In the second case, the deflection is shallow, and the melt pool is still in "forced conduction" mode.

5.1.2. KH absorptances at steady state

The computed KH absorptances at steady state are now compared to the apparent absorptances measured by Ye et *al.* [32], and to calibrated KH absorptances calculated by Grange et *al.* [38], and implemented in their numerical model of LPBF on Inconel® 738 LC. As a reminder, in the present work, only the material absorptance A_0 is calibrated. The KH apparent absorptance A is then computed self-consistently by the ray tracing algorithm as:

$$A = \frac{\int_S I_{abs} dS}{P_L} \tag{17}$$

In Grange's work [38], the initial (Gaussian) heat flux distribution imposed at liquid/gas interface is conserved, and the absorptance is adjusted so that the melt pool cross sections at steady state match the experimental bead cross section in KH mode. Also, the three datasets considered here were generated for different process parameters and varied materials. Therefore, to compare them rigorously, they are reported in a scaled map, using Ye's scaling law [32]:

$$A = \begin{cases} A_0, \dfrac{e}{R_L} \leq 1 \\ 0.70\left[1 - exp\left(-0.66\beta_{A_0} L^*_{th}\right)\right], \dfrac{e}{R_L} > 1 \end{cases} \tag{18}$$

where e is the KH depth, and β_{A_0} and L^*_{th} are respectively the normalized enthalpy and the normalized diffusion length:

$$\beta_{A_0} = \frac{A_0 P_L}{(T_{liq} - T_0)\pi\rho c_p \sqrt{\alpha V_L R_L^3}} \tag{19}$$

$$L^*_{th} = \sqrt{\frac{\alpha}{V_L R_L}} \tag{20}$$

where α is the thermal diffusivity. Note that in equation (18), the reference characteristic length used is the $1/e^2$ spot radius R_L, which is more consistent than the $1/e^2$ spot diameter. Also, it should be pointed out that the product $\beta_{A_0} L_{th}$ is proportional to the aspect ratio [39], which means that this parameter does characterize the evolution of the KH absorptance with its geometry (just like in Gouffé formula [40]).

Anyhow, if the experimental absorptances, our computed effective absorptances and the calibrated ones are equivalent (*i.e.*, if they refer to quantities of equivalent nature), they should all follow the same scaling law.

The results are plotted in Fig. 5. The experimental results, obtained for different experimental conditions all fit on the same curve, which demonstrate the "universal" character (*i.e.*, valid whatever the process parameters and material properties) of the scaling law. Our computed absorptances are also positioned on the same curve. As the KH depths were also validated, this means that the predicted KH shapes are also correct since there is a causal relationship between the KH depth, shape and absorptance [1]. However, the KH absorptances calibrated by Grange et *al.* [38] systematically overestimate the scaling law.

Several hypotheses may be formulated to explain this discrepancy. First, the results are sensible to the material properties (taken at melting temperature), especially to the assumed value of A_0, which is sensitive to the local temperature and oxidation. However, in Grange's work, $A_0 = 0.3$, which is consistent with Ye's measurements (minimum absorptance measured for liquid Inconel® 625: 0.28 [32]). Then, Grange's absorptances are calibrated in LPBF configuration, whereas our model and the experimental data were obtained on bare plates. However, for nickel alloys, the melt pool absorptances differ between powder bed and bare plate in "conduction" mode (due to partial wetting and coalescence of powder bed), but not in KH mode, where absorption is dominated by multiple reflections [32]. Hence, the presence of powder might not explain such high calibrated absorptance values.

The preferred hypothesis is that calibrating the apparent absorptance without modulating the distribution of the absorbed irradiance creates a discrepancy between the absorption level and the KH shape. Several numerical works [12,22] have shown that the absorbed irradiance is redistributed along the KH walls due to multiple reflections. This is clearly highlighted in Fig. 6, where irradiances absorbed along the scan path are compared, for $V_L = 400$ mm/s and $P_L = 250$ W. The red curve is computed with our simulation, whereas the black one, is calculated thanks to Grange's model (with $A = 0.8$), on the same KH geometry. Both models are normalized, taking Grange's result as reference. With the calibration method, the intensity absorbed at the KH bottom is underestimated, by a factor three in maximum, because multiple reflections are not explicitly accounted for. In other terms, Grange's method increases the average level of absorption, whereas multiple

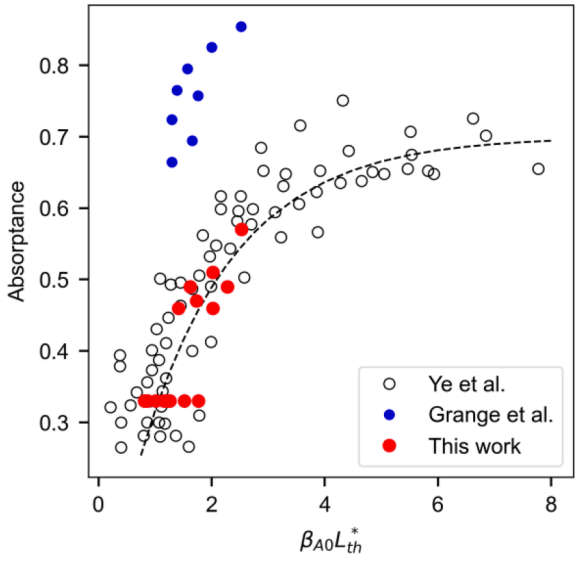

Fig. 5. Comparison of the computed KH absorptances (red solid circles) to experimental data (empty circles) published by Ye et al. [32] and calibrated absorptances (blue solid circles) computed by Grange et al. [38]. (For interpretation of the references to colour in this figure legend, the reader is referred to the web version of this article.)

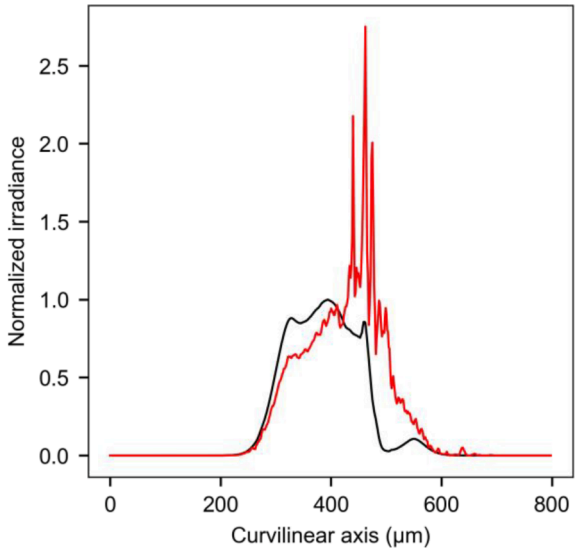

Fig. 6. Normalized irradiance absorbed along the scan path, for $V_L = 400$ W and $P_L = 250$ W. The black curve is calculated according to Grange's model [38] (calibration of apparent absorptance) and the red one is computed self consistently by our model. (For interpretation of the references to colour in this figure legend, the reader is referred to the web version of this article.)

reflections redistribute the irradiance locally, and determine the global KH shape. Therefore, calibrating the apparent absorptance to fit the bead cross section at steady state might be a pragmatic way to predict the actual melt pool dimensions, but the KH shape, thus, the KH absorptance, are not predicted consistently.

In the next section, the role of beam trapping on conduction-to-keyhole mechanisms, and on KH shape and stability are investigated through three case studies.

5.2. Analysis of conduction-to-keyhole transition

5.2.1. $V_L = 400$ mm/s, $P_L = 250$ W

In the first configuration, the scanning speed is low, and the incident power is high enough to get a stable KH mode at steady state. The sequence is illustrated in Fig. 7 (the animation is available in the complementary resources: supplementary video 2) and in complementary Fig. S1.

The first instants of this fusion mode are dominated by the same penetration mechanisms as in spot welding configuration (Fig. 7a-e). The KH initiates at constant aperture (about 100 μm): the "forced conduction" occurs mode at $t = 100$ μs (Fig. 7b), then, until $t = 200$ μs, the melt pool is destabilized by the horizontally reflected rays (Fig. 7c-d), and finally, when the deflection depth reaches the critical value of 50 μm (*i.e.*, aspect ratio = 1, which corresponds to a critical inclination of the KH front wall of 45°), the KH mode is initiated (Fig. 7e).

Afterward, at $t = 230$ μs, the KH takes his characteristic "V-shape", which is quasi-axisymmetric and remarkably similar to that observed in static mode (Fig. 7f). The KH walls oscillates as long as the aperture-to-depth ratio is close to one. It is shown in the supplementary Fig. S1 that the absorptance vs time curve also oscillate during this period, which is

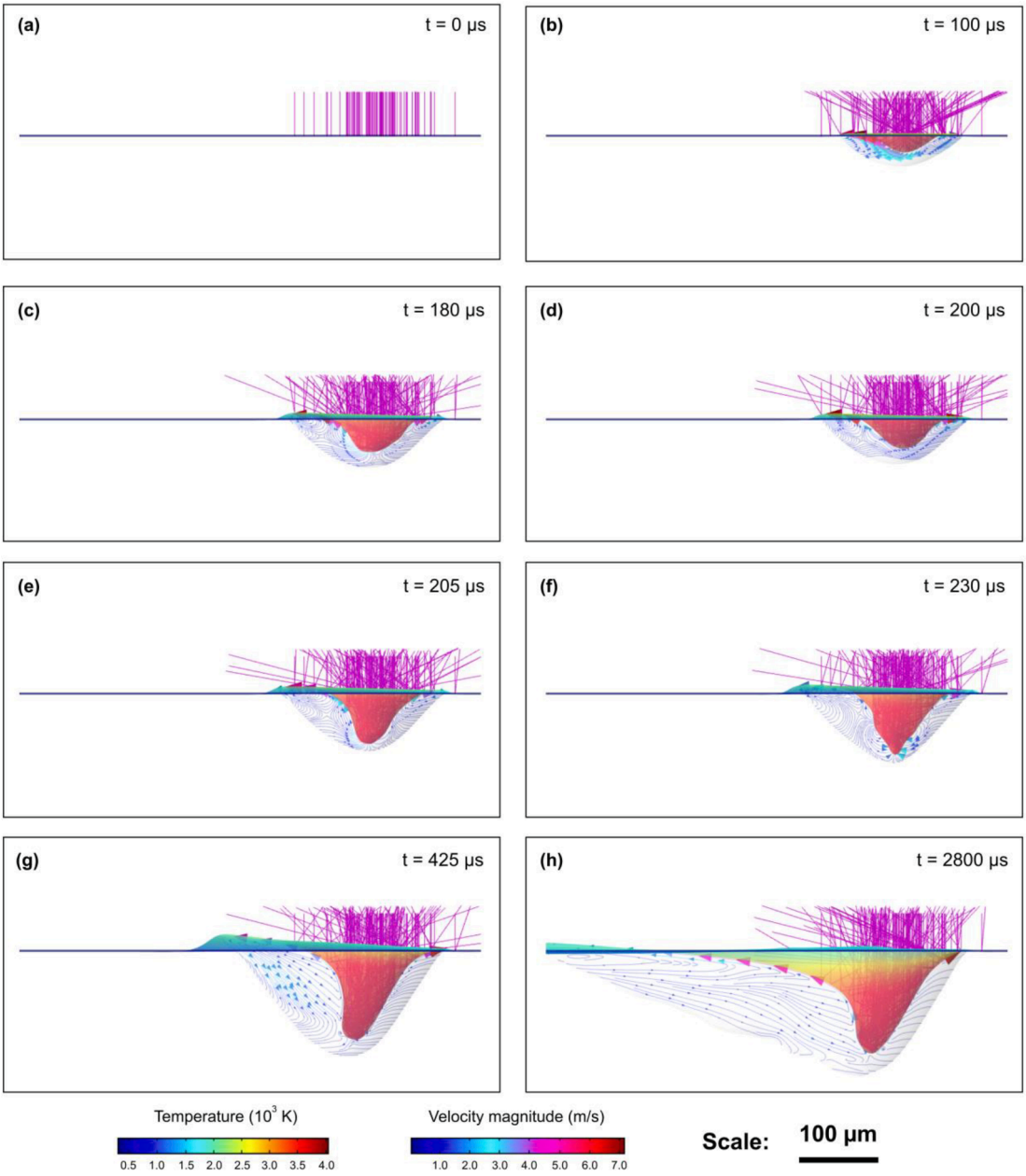

Fig. 7. KH formation sequence for $V_L = 400$ mm/s and $P_L = 250$ W. **a.** Laser irradiation starts. **b.** The "forced conduction" mode starts. **c-d.** Laser beam is progressively reflected horizontally, which makes the melt pool fluctuate. **e.** The incident rays are reflected bottomward; therefore, the KH mode is initiated. **f.** The KH oscillate. Its shape is very analogous to that observed during the spot welding mode. **g.** The KH continues to deepen and reaches 90 % of its steady value. **h.** The KH aperture (in the scanning direction) gets wider at the sample surface, but the "effective" aperture is constant.

consistent with the causal relationship between the KH geometry and absorptance, highlighted by Simonds et *al.* [1]. When this critical aperture-to-depth ratio is exceeded, the KH stabilizes, and at $t = 425$ µs, its depth reaches about 90 % of the steady value of 130 µm (Fig. 7g).

Finally, only after the above sequence is finished, the KH rear wall gets its final position (Fig. 7h). Consequently, the KH aperture (in the scanning direction) at the sample surface is 450 µm wide, but the "effective" aperture (*i.e.*, the part of the cavity which effectively traps the incident beam) is still of 100 µm at steady state, which is consistent with the critical depression width identified by Cunningham et *al.* [8] in the same conditions.

In short, in this process configuration, the melt pool dynamics is dominated by the KH penetration mechanisms (also shown by superimposed contours of liquid/gas interfaces available in Fig. S1). The resulting melt pool is very stable (except, at transient state, around the critical aspect ratio) and has analogous characteristics to the so-called "pre-humping" regime described by Fabbro [41] – stable KH with strong backflow emerging from the bottom KH to the initial sample surface, and a relatively low KH front wall angle, here about 30° (relative to the laser axis).

5.2.2. $V_L = 700$ mm/s, $P_L = 350$ W

In this second configuration, the scan speed is higher than in the previous case, and the laser power is set to get a KH depth at steady state, close to the critical depression width of 100 µm. The KH formation sequence is illustrated in Fig. 8 (the animation is available in the complementary resources: supplementary video 3) and in supplementary Fig. S2.

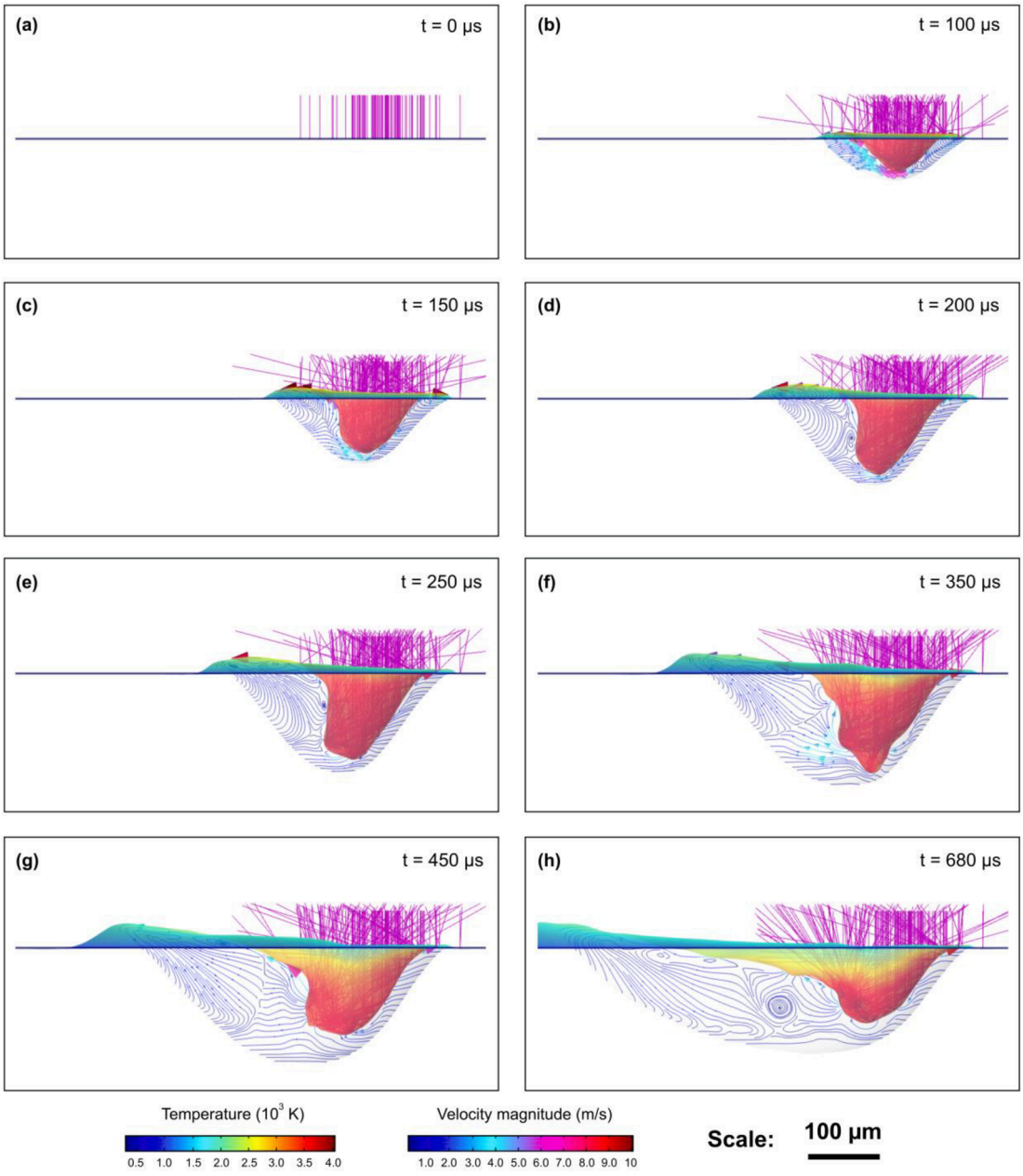

Fig. 8. KH formation sequence for $V_L = 700$ mm/s and $P_L = 350$ W. **a.** Laser irradiation starts. **b-c.** The KH mode initiates as the rays are progressively reflected bottomward. **d-e.** The incident rays are reflected on the KH rear wall, which is vertical. Consequently, the recoil pressure is exerted bottomward and rearward. **f.** The KH depth reaches its maximum value. However, its rear wall is pushed backward by the recoil pressure. Consequently, the KH opens and enters a very unstable phase. **g-h.** When opening due to the recoil pressure, the KH energy coupling is being reduced. Therefore, the final KH and melt pool depths are lower than their maximum value over time.

In this fusion mode, the drilling and opening mechanisms compete. First, during the first 200 μs, the process is very analogous to the previous case, except that the cavity is more titled toward the welding direction, at 40° relative to the laser axis (Fig. 8a-d). This is due to the higher scanning speed. Consequently, the incident rays are reflected toward the KH rear wall, which is vertical. The local temperature thus increases at this location because the absorption of the reflected rays is maximized at normal incidence. Therefore, the recoil pressure pushes the KH rear wall backward (Fig. 8e).

Then, between $t = 250$ μs and $t = 350$, the KH depth reaches a local maximum of 130 μm (Fig. 8f). However, as the cavity is being opened by the recoil pressure, the number of multiple reflections decreases, and the KH depth drop progressively toward its steady value of 105 μm (*i.e.*, above the conduction-to-keyhole threshold, but near the critical depression width), with an inclination of the KH front of 35°. The transition between these two states results here, in strong KH fluctuations (Fig. 8f-h). Note that the absorptance vs time curve exhibits the exact same behavior (Fig. S2).

To the best of the author's knowledge, existence of these two distinct phases (*i.e.*, formation of a deep and narrow KH, followed by a shallow and open one) at constant welding speed has not been clearly simulated and explained before. This effect was recently filmed by Simonds et *al.* [1] by X-ray imaging. To explain this phenomenon, they assumed that during the first phase (*i.e.*, deep, and narrow KH), the vapor plume exerts a friction force on the KH rear wall, which moves the liquid metal away from the interaction zone. The vapor plume would then lower the height of the KH rim, which in turn, reduces the number of multiple reflections and hence, lowers the KH depth. However here, the vapor plume is not integrated in the model, but the phenomenon is still observed.

An alternative hypothesis is thus formulated here. At first order, it involves the competition between the KH penetration and opening mechanisms. During the early stage of KH formation, the melt is ejected rearward by the recoil pressure. However, the solidification front is still close to the interaction zone, so the melt accumulates, forming a protrusion at the back of the melt pool. Consequently, the liquid metal cannot be moved away from the interaction zone, which favors multiple reflections and KH penetration. Then, as the beam travels, the melt pool length growths, which enables the KH to open, depending on the scanning velocity (the higher the scanning velocity, the longer the KH aperture) and on the ejection velocity, being driven by the recoil pressure. The multiple reflections effect contributes to open the KH during this second stage, at the expense of KH penetration. The vapor plume may also contribute to the mechanism (if it is oriented toward the KH rear front), but it is not the main driving force.

Finally note that in the present case, the observed regime change is less significant than in Simonds' work. In our case, the depth and absorptance shifts are only of 20 %, whereas in Simonds' case, it is of about 65 % [1]. One reason is that in our simulation, power ramping is implemented to ensure numerical stability. Without power ramping, the KH would have been deeper during the first phase, so the effect would have been more pronounced.

5.2.3. $V_L = 1000$ mm/s, $P_L = 350$ W

In the last configuration, the laser power is kept at 350 W, but the scan speed is increased to 1000 mm/s, so that the KH depth at steady state is below the critical depression width of 100 μm. The sequence is illustrated in Fig. 9 (the animation is available in the complementary resources: supplementary video 4) and in Fig. S3.

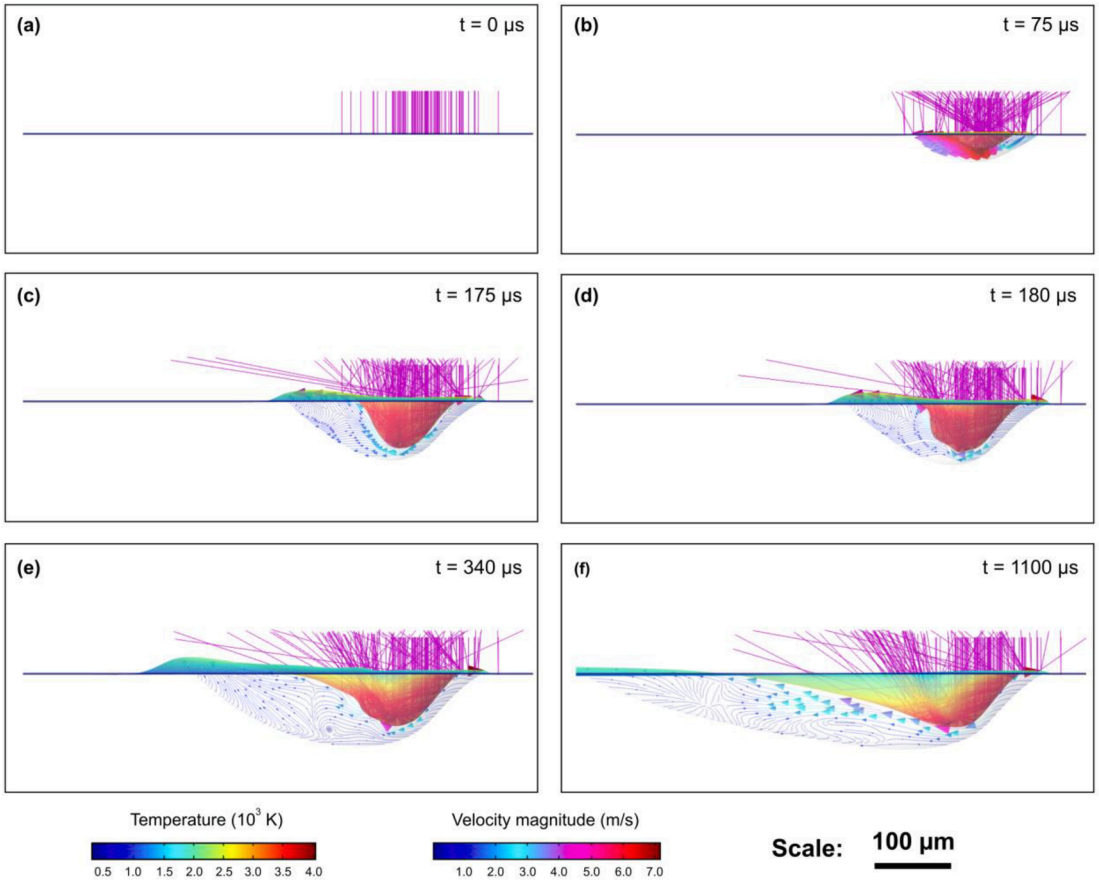

Fig. 9. KH formation sequence for $V_L = 1000$ mm/s and $P_L = 350$ W. **a-b.** The liquid/gas deflection forms progressively. The melt pool is in "forced conduction" mode. **c-d.** The rays are reflected horizontally; therefore, the rear wall of the deflection (which becomes vertical) is pushed back by the recoil pressure. **e.** The deflection depth has reached its steady value, but the aperture continues to widen, as a result of the melt flow. **f.** The steady state is reached.

At the beginning of the sequence, the depth of the cavity is sufficient to initiate melt pool destabilization, because the incident rays are reflected horizontally (Fig. 9a-c). As in the previous case, the absorptance vs time curve also oscillates during this stage, but at lower amplitude and frequency (Fig. S3). However, the steady depth is rapidly reached, while the deflection continues to widen, due to the higher welding speed. This stabilizes the melt pool since the reflected rays are absorbed at lower incident angles. Also, like in the previous configuration, the reflected rays contribute to keep the melt deflection open (Fig. 9d-e), but the final shape of the liquid/gas interface is mainly the result of the melt flow, which is strongly directed rearward (Fig. 9f). The steady KH depth is then equal to 65 μm, which corresponds to an inclination of the KH front of 40°.

Recent findings [2,24] suggest that if the inclination of the KH front wall is equal de 45° at steady state (*i.e.*, KH threshold), then the KH instabilities are maximized. The KH then oscillates between the "forced conduction" mode and the KH mode, causing high fluctuations in the melt pool depth along the scan path, and large spatters. This particular melt pool state was also described about thirty years ago by Zhang et *al.*, [42] (and called "Unstable Mode Welding"). Here, we demonstrate that the melt pool stability is also strongly dependent on the KH aperture, both being increased by the scanning speed. Therefore, similar to Fabbro [2], we deduce that this particular fusion mode is expected to occur when the KH rear wall is close to the KH front, at lower scan speed, when the ejection velocity is not high enough to move the liquid metal away from the interaction zone.

6. Conclusion

The objective of this work was to study the physical mechanisms that drive the conduction-to-keyhole transition during laser processing. For that purpose, a thermo-hydrodynamic finite element model was developed with COMSOL Multiphysics®, where the absorbed laser irradiance is computed self consistently, thanks to a ray tracing algorithm. After validating the model in various configurations (transient KH depth vs time in spot welding mode, steady KH depths and apparent absorptances in welding configuration), different findings were presented. The main ones are summarized as follows:

- In spot welding configuration, conduction-to-keyhole transition occurs at constant KH aperture, fixed by the laser spot size. Therefore, at given spot size, the KH mode initiates when the deflection of the liquid/gas interface reaches a threshold depth-to-aperture ratio, independent to the laser power.
- In welding configuration, when the incident beam is Gaussian, the conduction-to-keyhole transition occurs when the deflection of liquid/gas interface reaches a threshold depth, equals to the $D_{1.35\sigma}$ diameter (*i.e.*, the width which account for 50 % of the incident energy), corresponding to a critical inclination of the front KH of 45°. This result confirms the traditional definition of the KH threshold reached when its aspect ratio exceeds the value of one.
- Competition between KH penetration and KH opening, plays a determinant role on the KH stability during the conduction-to-keyhole process in scanning laser processing:
  - o At lower scan speeds, the penetration mechanism (driven by the recoil pressure, emphasized by the multiple reflections) dominates the process. The resulting KH is relatively narrow and stable.
  - o At higher scan speed, on contrary, the opening mechanisms dominate (driven by the melt flow, strongly directed rearward, and helped by rearward reflections). The resulting KH is shallow, elongated, and stable.
  - o At intermediate speeds, there are configurations where, a deep and narrow KH is formed during the first stage of melting, followed by a shallow and open KH at the end of the track. The KH stability increases with its aperture.
- Finally, a self-consistent beam energy deposition model is needed to simulate the KH dynamics and absorptance. Calibrating the latter to fit the seam cross sections at steady state leads to overestimate the actual physical absorptances.

To complete this work, we suggest running simulations around the KH threshold at different welding speeds, with thinner process parameter steps. Doing so, accurate KH stability conditions – on KH aperture and front wall angle – can be defined. Particularly, it would be interesting to simulate the "Unstable Mode Welding", which will be possible with Eulerian front capturing methods (such as Level-Set or Phase Field methods). Future X-ray experiments could also focus on this thematic, to help welders and additive manufacturers to identify their stable process windows.

CRediT authorship contribution statement

Yaasin A. Mayi: Conceptualization, Methodology, Software, Validation, Investigation, Visualization, Writing - original draft. **Morgan Dal:** Supervision, Funding acquisition, Project administration, Conceptualization, Writing - review & editing. **Patrice Peyre:** Supervision, Conceptualization, Writing - review & editing. **Michel Bellet:** Supervision, Conceptualization, Writing - review & editing. **Remy Fabbro:** Conceptualization, Supervision, Writing - review & editing.

Declaration of Competing Interest

The authors declare that they have no known competing financial interests or personal relationships that could have appeared to influence the work reported in this paper.

Data availability

The data that has been used is confidential.

Acknowledgement

The authors would like to thank Alexis Queva (co-author of Grange et *al.* [38]) for his help in interpreting the differences between the calibrated and the self-consistent absorptances. This work was supported by the company Safran and by Association Nationale de la Recherche et de la Technologie (ANRT), under the Grant No. 2017/1290.

Appendix A. Supplementary data

Supplementary data to this article can be found online at https://doi.org/10.1016/j.optlastec.2022.108811.

References

[1] B.J. Simonds, J. Tanner, A. Artusio-Glimpse, P.A. Williams, N. Parab, C. Zhao, T. Sun, The causal relationship between melt pool geometry and energy absorption measured in real time during laser-based manufacturing, Appl. Mater. Today 23 (2021), 101049, https://doi.org/10.1016/j.apmt.2021.101049.
[2] R. Fabbro, Depth Dependence and Keyhole Stability at Threshold, for Different Laser Welding Regimes, Applied Sciences. 10 (2020) 1487, https://doi.org/10.3390/app10041487.
[3] V. Semak, A. Matsunawa, The role of recoil pressure in energy balance during laser materials processing, J. Phys. D: Appl. Phys. 30 (1997) 2541–2552, https://doi.org/10.1088/0022-3727/30/18/008.
[4] Y.A. Mayi, A. Queva, M. Dal, G. Guillemot, C. Metton, C. Moriconi, P. Peyre, M. Bellet, Multiphysics simulation of single pulse laser powder bed fusion: comparison of front capturing and front tracking methods, HFF. 32 (2022) 2149–2176, https://doi.org/10.1108/HFF-04-2021-0282.
[5] H. Ki, P.S. Mohanty, J. Mazumder, Modelling of high-density laser-material interaction using fast level set method, J. Phys. D: Appl. Phys. 34 (2001) 364–372, https://doi.org/10.1088/0022-3727/34/3/320.
[6] J.Y. Lee, S.H. Ko, D.F. Farson, C.D. Yoo, Mechanism of keyhole formation and stability in stationary laser welding, J. Phys. D: Appl. Phys. 35 (2002) 1570–1576, https://doi.org/10.1088/0022-3727/35/13/320.

[7] M. Medale, C. Touvrey, R. Fabbro, An axi-symmetric thermo-hydraulic model to better understand spot laser welding, European Journal of Computational Mechanics. 17 (2008) 795–806, https://doi.org/10.3166/remn.17.795-806.

[8] R. Cunningham, C. Zhao, N. Parab, C. Kantzos, J. Pauza, K. Fezzaa, T. Sun, A. D. Rollett, Keyhole threshold and morphology in laser melting revealed by ultrahigh-speed x-ray imaging, Science 363 (2019) 849–852, https://doi.org/10.1126/science.aav4687.

[9] B.J. Simonds, J. Sowards, J. Hadler, E. Pfeif, B. Wilthan, J. Tanner, C. Harris, P. Williams, J. Lehman, Time-Resolved Absorptance and Melt Pool Dynamics during Intense Laser Irradiation of a Metal, Phys. Rev. Applied. 10 (2018), 044061, https://doi.org/10.1103/PhysRevApplied.10.044061.

[10] T.R. Allen, W. Huang, J.R. Tanner, W. Tan, J.M. Fraser, B.J. Simonds, Energy-Coupling Mechanisms Revealed through Simultaneous Keyhole Depth and Absorptance Measurements during Laser-Metal Processing, Phys. Rev. Applied. 13 (2020), 064070, https://doi.org/10.1103/PhysRevApplied.13.064070.

[11] L. Wang, Y. Zhang, W. Yan, Evaporation Model for Keyhole Dynamics During Additive Manufacturing of Metal, Phys. Rev. Applied. 14 (2020), 064039, https://doi.org/10.1103/PhysRevApplied.14.064039.

[12] Y.A. Mayi, M. Dal, P. Peyre, M. Bellet, C. Metton, C. Moriconi, R. Fabbro, Transient dynamics and stability of keyhole at threshold in laser powder bed fusion regime investigated by finite element modeling, J. Laser Appl. 33 (1) (2021) 012024.

[13] M. Wei, W.J. Ding, G. Vastola, Y.-W. Zhang, Quantitative study on the dynamics of melt pool and keyhole and their controlling factors in metal laser melting, Addit. Manuf. 54 (2022), 102779, https://doi.org/10.1016/j.addma.2022.102779.

[14] M. Courtois, M. Carin, P. Le Masson, S. Gaied, M. Balabane, Guidelines in the experimental validation of a 3D heat and fluid flow model of keyhole laser welding, J. Phys. D: Appl. Phys. 49 (15) (2016) 155503.

[15] S. Pang, X. Chen, X. Shao, S. Gong, J. Xiao, Dynamics of vapor plume in transient keyhole during laser welding of stainless steel: Local evaporation, plume swing and gas entrapment into porosity, Opt. Lasers Eng. 82 (2016) 28–40, https://doi.org/10.1016/j.optlaseng.2016.01.019.

[16] C. Tang, J.L. Tan, C.H. Wong, A numerical investigation on the physical mechanisms of single track defects in selective laser melting, Int. J. Heat Mass Transf. 126 (2018) 957–968, https://doi.org/10.1016/j.ijheatmasstransfer.2018.06.073.

[17] M. Bayat, A. Thanki, S. Mohanty, A. Witvrouw, S. Yang, J. Thorborg, N.S. Tiedje, J. H. Hattel, Keyhole-induced porosities in Laser-based Powder Bed Fusion (L-PBF) of Ti6Al4V: High-fidelity modelling and experimental validation, Addit. Manuf. 30 (2019), 100835, https://doi.org/10.1016/j.addma.2019.100835.

[18] W. Yuan, H. Chen, T. Cheng, Q. Wei, Effects of laser scanning speeds on different states of the molten pool during selective laser melting: Simulation and experiment, Mater. Des. 189 (2020), 108542, https://doi.org/10.1016/j.matdes.2020.108542.

[19] C. Tang, K.Q. Le, C.H. Wong, Physics of humping formation in laser powder bed fusion, Int. J. Heat Mass Transf. 149 (2020), 119172, https://doi.org/10.1016/j.ijheatmasstransfer.2019.119172.

[20] H. Wang, Y. Zou, Microscale interaction between laser and metal powder in powder-bed additive manufacturing: Conduction mode versus keyhole mode, Int. J. Heat Mass Transf. 142 (2019), 118473, https://doi.org/10.1016/j.ijheatmasstransfer.2019.118473.

[21] B. Liu, G. Fang, L. Lei, W. Liu, Experimental and numerical exploration of defocusing in Laser Powder Bed Fusion (LPBF) as an effective processing parameter, Opt. Laser Technol. 149 (2022), 107846, https://doi.org/10.1016/j.optlastec.2022.107846.

[22] N. Kouraytem, X. Li, R. Cunningham, C. Zhao, N. Parab, T. Sun, A.D. Rollett, A. D. Spear, W. Tan, Effect of Laser-Matter Interaction on Molten Pool Flow and Keyhole Dynamics, Phys. Rev. Applied. 11 (2019), 064054, https://doi.org/10.1103/PhysRevApplied.11.064054.

[23] E. Li, Z. Zhou, L. Wang, R. Zou, A. Yu, Modelling of keyhole dynamics and melt pool flow in laser powder bed fusion process, Powder Technol. 400 (2022), 117262, https://doi.org/10.1016/j.powtec.2022.117262.

[24] A.A. Martin, N.P. Calta, J.A. Hammons, S.A. Khairallah, M.H. Nielsen, R. M. Shuttlesworth, N. Sinclair, M.J. Matthews, J.R. Jeffries, T.M. Willey, J.R.I. Lee, Ultrafast dynamics of laser-metal interactions in additive manufacturing alloys captured by in situ X-ray imaging, Materials Today Advances. 1 (2019), 100002, https://doi.org/10.1016/j.mtadv.2019.01.001.

[25] C.J. Knight, Theoretical Modeling of Rapid Surface Vaporization with Back Pressure, AIAA Journal. 17 (1979) 519–523, https://doi.org/10.2514/3.61164.

[26] V.R. Voller, C. Prakash, A fixed grid numerical modelling methodology for convection-diffusion mushy region phase-change problems, Int. J. Heat Mass Transf. 30 (1987) 1709–1719, https://doi.org/10.1016/0017-9310(87)90317-6.

[27] COMSOL Multiphysics® v 5.5, (2020). www.comsol.com.

[28] Y.A. Mayi, M. Dal, P. Peyre, C. Metton, C. Moriconi, R. Fabbro, An Original Way of Using COMSOL® Application Builder to Enhance Multiphysical Simulation of Laser Welding Processes, in: Proceedings of the COMSOL European Conference 2020, Grenoble, 2020.

[29] Y.A. Mayi, Compréhension et simulation des phénomènes physiques affectant la fabrication additive en SLM, École Nationale Supérieure d'Arts et Métiers (2021), https://doi.org/10.6084/m9.figshare.17158226.v3.

[30] C. Touvrey-Xhaard, Étude thermohydraulique du soudage impulsionnel de l'alliage TA6V, Université de Provence - Aix-Marseille I, 2006.

[31] M. Geiger, K.-H. Leitz, H. Koch, A. Otto, A 3D transient model of keyhole and melt pool dynamics in laser beam welding applied to the joining of zinc coated sheets, Prod. Eng. Res. Devel. 3 (2009) 127–136, https://doi.org/10.1007/s11740-008-0148-7.

[32] J. Ye, S.A. Khairallah, A.M. Rubenchik, M.F. Crumb, G. Guss, J. Belak, M. J. Matthews, Energy Coupling Mechanisms and Scaling Behavior Associated with Laser Powder Bed Fusion Additive Manufacturing, Adv. Eng. Mater. 21 (2019) 1900185, https://doi.org/10.1002/adem.201900185.

[33] K.C. Mills, Recommended values of thermophysical properties for selected commercial alloys, Woodhead, Cambridge, 2002.

[34] J.A. Dean, N.A. Lange, Lange's handbook of chemistry, 15th ed., McGraw-Hill, New York, 1999.

[35] Titanium/Aluminium/Vanadium (Ti90/Al 6/V4), Goodfellow. (2021). https://www.goodfellow.com/E/Titanium-Aluminium-Vanadium-Alloy.html.

[36] K. Zhou, B. Wei, Determination of the thermophysical properties of liquid and solid Ti–6Al–4V alloy, Appl. Phys. A. 122 (2016) 248, https://doi.org/10.1007/s00339-016-9783-6.

[37] R. Fabbro, M. Dal, P. Peyre, F. Coste, M. Schneider, V. Gunenthiram, Analysis and possible estimation of keyhole depths evolution, using laser operating parameters and material properties, J. Laser Appl. 30 (3) (2018) 032410.

[38] D. Grange, A. Queva, G. Guillemot, M. Bellet, J.-D. Bartout, C. Colin, Effect of processing parameters during the laser beam melting of Inconel 738: Comparison between simulated and experimental melt pool shape, J. Mater. Process. Technol. 289 (2021), 116897, https://doi.org/10.1016/j.jmatprotec.2020.116897.

[39] R. Fabbro, Scaling laws for the laser welding process in keyhole mode, J. Mater. Process. Technol. 264 (2019) 346–351, https://doi.org/10.1016/j.jmatprotec.2018.09.027.

[40] A. Gouffé, Corrections d'ouverture des corps noirs artificiels compte tenu des diffusions multiples internes, Revue d'optique. 24 (1945) 1–10.

[41] R. Fabbro, Melt pool and keyhole behaviour analysis for deep penetration laser welding, J. Phys. D: Appl. Phys. 43 (44) (2010) 445501.

[42] X. Zhang, W. Chen, J. Ren, Y. Wang, G. Huang, H. Zhang, Effects of processing parameters on mode and stability of laser welding, in: J.J. Dubowski, J. Mazumder, L.R. Migliore, C. Roychoudhuri, R.D. Schaeffer (Eds.), San Jose, CA, 1996: p. 343. https://doi.org/10.1117/12.237746.